

A Herschel–Bulkley model for mud flow down a slope

By XIN HUANG AND MARCELO H. GARCÍA

Hydrosystems Laboratory, Department of Civil and Environmental Engineering,
University of Illinois, Urbana, IL 61801, USA
email: mhgarcia@uiuc.edu

(Received 20 May 1997 and in revised form 15 June 1998)

The spreading and sediment deposit of a two-dimensional, unsteady, laminar mud flow from a constant-volume source on a relatively steep slope is studied theoretically and experimentally. The mud under consideration has the rheological properties of a Herschel–Bulkley fluid. The flow is of low-Reynolds-number type and has a well-formed wave front moving a substantial distance downslope. Due to the nonlinear rheological characteristics, a set of nonlinear partial differential equations is needed for this transient problem. Depth-integrated continuity and momentum equations are derived by applying von Kármán's momentum integral method. A matched-asymptotic perturbation method is implemented analytically to get asymptotic solutions for both the outer region away from, and the inner region near, the wave front. The outer solution gives accurate results for spreading characteristics, while the inner solution, which is shown to agree well with experimental results of Liu & Mei (1989) for a Bingham fluid, predicts fairly well the free-surface profile near the wave front. A composite solution uniformly valid over the whole spreading length is then achieved through a matching of the inner and outer solutions in an overlapping region. The range of accuracy of the solution and the size of the inner and overlapping regions are quantified by physical scaling analyses. Rheological and dynamic measurements are obtained through laboratory experiments. Theoretical predictions are compared with experimental results, showing reasonable agreement. The impact of shear thinning on the runout characteristics, free-surface profiles and final deposit of the mud flow is examined. A mud flow with shear thinning spreads beyond the runout distance estimated by a Bingham model, and has a long and thin deposit.

1. Introduction

Mud flows are commonly observed in mountainous areas after long or intense rainy periods, inflicting significant topographical changes when debouching over the associated alluvial fans (Johnson 1970; Li *et al.* 1983; Costa & Williams 1984; Takahashi 1991). These flows also occur frequently as mud-slides on submarine continental slopes where they play an important role in geological processes (Hampton, Lee & Locat 1996; Huang & García 1998). Therefore, it is of interest to be able to predict the characteristics (e.g. runout extent) of mud flows and their deposits for geophysical and engineering purposes. To this end, complete, proper, constitutive relations for muds must be taken into account as well as appropriate boundary and initial conditions.

Rheological studies of mud at high enough solid concentrations have shown that it is a very viscous, non-Newtonian fluid (Krone 1963; Migniot 1968; Wan 1982;

Cases	C_v (%)	Bingham plastic (Wan 1982)		Herschel–Bulkley (present study)		n
		τ_y (N m ⁻²)	μ (N m ⁻² s)	τ_y (N m ⁻²)	μ (N m ⁻² s ^{n})	
(1)	14.9	5.178	0.00889	2.800	0.910	0.30
(2)	12.6	2.764	0.00638	2.100	0.090	0.59
(3)	10.5	1.424	0.00488	0.875	0.095	0.54
(4)	7.4	0.499	0.00358	0.085	0.080	0.50

τ_y is the yield stress, μ the kinematic viscosity and n is given by (2.10).

TABLE 1. Rheological parameters for kaolinite suspension (Wan 1982)

Coussot 1994), exhibiting a yield stress as evidenced by an observed minimum depth needed for a uniform layer of mud to flow. Various rheological models have been proposed (e.g. Bird, Dai & Yarusso 1983), and the most often used one for the shear rate range seen in natural rivers and on alluvial fans (Johnson 1970; Qian & Wan 1986) is the Bingham plastic model (also called linear viscoplastic model). Following numerous field studies, Qian & Wan (1986) indicated that the shear rate of a high-density mud flow in natural rivers is generally no more than 100 s⁻¹ and this should be kept in mind when using data from rheological measurements. This is true for a lava flow or a mud flow at a decelerating stage on an alluvial fan. For example, Li *et al.* (1983) measured the following data for a mud flow in Jiang-jia Ravine, China: density $\rho = 2.13$ g cm⁻³, slope $\sin \theta = 0.06$, depth $h = 1.4$ m, surface velocity $u(h) = 8.0$ m s⁻¹, and yield stress $\tau_y = 2000$ – 3000 dynes cm⁻². A Bingham plastic simulation (Huang & García 1997*b*) estimates a kinematic viscosity $\mu/\rho \approx 0.047$ m² s⁻¹, a basal shear rate ≈ 15 s⁻¹, a depth-averaged velocity ≈ 5.7 m s⁻¹, a Reynolds number ≈ 500 , and a Froude number ≈ 1.5 . However, very large shear rates are bound to exist in mud flows at the accelerating stage in mountainous areas. Also, it has been found that yielded mud may experience shear thinning at low shear stress level, i.e. its viscosity decreases gradually with the increase of shear rate. This is probably because the destruction of the internal structure responsible for the yield behaviour is a gradual process, during which the resistance to deformation becomes weaker, and is not completed until a high shear stress level is reached. Therefore, a Bingham plastic model may overestimate the true yield stress significantly due to the shear thinning at low shear rates (Wan 1982; O'Brien & Julien 1988), and muds with high solid concentrations generally experience more severe shear thinning than those with low solid concentrations (see table 1 and figure 1). A Herschel–Bulkley model (also called a nonlinear viscoplastic model, see Coussot 1997) seems to be more appropriate in depicting this particular behaviour and is found to fit rheological data very well over a wide range of shear rates (figure 1).

In simple shear, the stress and strain relation for a Herschel–Bulkley fluid in laminar flows is

$$\mu_n \left| \frac{\partial u}{\partial y} \right|^n \operatorname{sgn} \left(\frac{\partial u}{\partial y} \right) = \begin{cases} 0 & \text{if } |\tau| < \tau_y, \\ \tau - \tau_y \operatorname{sgn} \left(\frac{\partial u}{\partial y} \right) & \text{if } |\tau| \geq \tau_y \end{cases} \quad (1.1)$$

where τ is the shear stress, τ_y is the yield stress, μ_n is the dynamic viscosity of dimension $[ML^{-1}T^{n-2}]$, and n is the flow index ranging between 0 and 1 for a shear-thinning fluid. The upper limit of $n = 1$ corresponds to a Bingham plastic fluid, and μ_1 is the regular dynamic viscosity. The existence or non-existence of the yield stress has recently been

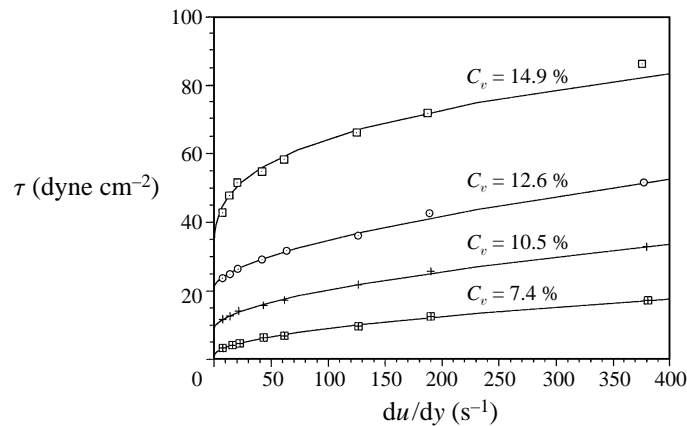


FIGURE 1. The rheological measurements for kaolinite suspension (Wan 1982), fitted by the Herschel–Bulkley model.

the subject of discussion (e.g. Barnes & Walters 1985; Evans 1992; Schurz 1992; Kee & Fong 1993; Spanns & Williams 1995). It is true that dense muds deform, however slowly, under the action of small shear stresses. However, Nguyen & Boyer (1992) questioned the measurements by Barnes & Walters in that all rheometers suffer wall slip and other side effects (e.g. particle dispersion) especially at low shear rates and for yield-stress fluids and particle suspensions. They further pointed out that, under common conditions of observation, there generally exists an abrupt turn in the deformation rate of dense mud from an elastic/plastic solid behaviour to a viscous fluid behaviour, when shear stress exceeds a certain value that we can call the yield stress. Nevertheless, there must be fluid materials (e.g. dilute clay suspensions) which do not possess yield stress and may follow a power law (Ng & Mei 1994), and this can be treated as a special case of a Herschel–Bulkley model. The yield stress may lead to two fluid regions: a sheared one with $\tau > \tau_y$ and varying velocity, and an unsheared one with $\tau \leq \tau_y$ and uniform velocity, for flows in simple geometries (Lipscomb & Denn 1984; Piau 1996). The dynamic problem of a yield-stress fluid flow has the interface between the two regions as a boundary condition unknown *a priori*, whose location has to be determined together with other unknowns (Bird *et al.* 1983; Crochet & Walters 1983).

Although there has been substantial research carried out on free-surface flows of Newtonian viscous fluids, much less has been done for yield-stress fluids, either experimentally or theoretically, with most of the work concentrating on flows in simple geometries and steady state or transient slow motions (Liu & Mei 1989, 1990; Coussot 1997). Linear instability analyses of uniform flows of dense mud include Engelund & Wan (1984), Trowbridge (1987), Hjorth (1990), Liu & Mei (1994), and Ng & Mei (1994). Recently, the slow, unconfined spreading of a mud flow coming out of a narrow open channel was investigated using a three-dimensional form of the constitutive equation (Coussot & Proust 1996). The form of the deposits remaining after a free-surface flow stops was found to be a function of fluid characteristics (Coussot, Proust & Ancey 1996). More recently, the propagation of a constant-volume mud source encountered in a dam-break or mud-slide problem was analysed by using the matched-asymptotic perturbation method (Huang & García 1997*b*). In this last problem, however, the effect of shear thinning (i.e. the flow index n) on the runout characteristics and final deposits of mud flows was not studied. Shear thinning should have an impact on flow properties which have engineering and geophysical importance. Motivated by

this fact, the formulation corresponding to the work of Huang & García (1997*b*) will be given more rigorously in what follows for Herschel–Bulkley fluids with a focus on the shear-thinning effects.

The mud flows being considered here are laminar flows as often encountered in nature for highly concentrated suspensions. As far as we know, no criterion for the transition from a laminar to a turbulent regime exists for fluids following a Herschel–Bulkley model. But there are several empirical criteria proposed for free-surface flows of Bingham fluids (Wilkinson 1960; Qian & Wan 1986; Naik 1983) which may at the very least give an approximate idea of how far the flows under consideration are from the transition zone. To this end, the criterion used by Qian & Wan (1986) for mud flows is used by fitting the rheological data with a Bingham model:

$$\frac{1}{Re_B} = \frac{1}{Re_\tau} + \frac{1}{Re_\mu} \quad (1.2)$$

with $Re_\tau = 8\rho U^2/\tau_y$ and $Re_\mu = 4\rho Uh/\mu$. (1.3)

Empirically, for a mud flow to remain laminar, $Re_B < 2100$, and it will be verified *a posteriori* that the mud flows considered later in this paper are indeed laminar.

In this paper, the dynamics of a mud flow which originates from a constant-volume source on a relatively steep slope and follows the Herschel–Bulkley rheological behaviour is formulated with the help of the boundary-layer approximations. The flow is of low-Reynolds-number type and has a substantial runout distance. The derived governing equations are then solved analytically by using the method of matched-asymptotic expansions. The impact of shear thinning on the spreading characteristics, free-surface profiles and final deposit is examined. Two special cases of the analytical solution have been verified experimentally by previous investigations: the Bingham model (Liu & Mei 1989; Huang & García 1997*a, b*) and the Newtonian model (Huppert 1982*a*, 1986; Hunt 1994). Experimental results on Herschel–Bulkley mud flow are also shown in this study. Finally, some practical considerations concerning the application of the solution are discussed.

2. Governing equations: boundary-layer approximations

Consider a two-dimensional, unsteady, gradually varied, laminar mud flow down a relatively steep slope at an angle θ with respect to the horizontal. A coordinate system (x, y) is defined as the x -axis downslope along and the y -axis upward normal to the plane bed. The longitudinal and transverse velocity components are denoted by (u, v) , the pressure by p , and the total flow depth normal to the bed by h . The boundary-layer approximations are assumed to be valid, i.e. the characteristic flow depth is small relative to the characteristic flow length and the flow depth changes relatively slowly in the longitudinal direction. Then the flow is governed by the boundary-layer approximation equations

$$\frac{\partial u}{\partial x} + \frac{\partial v}{\partial y} = 0, \quad (2.1)$$

$$\frac{\partial u}{\partial t} + u \frac{\partial u}{\partial x} + v \frac{\partial u}{\partial y} = -\frac{1}{\rho} \frac{\partial p}{\partial x} + g \sin \theta + \frac{1}{\rho} \frac{\partial \tau}{\partial y}, \quad (2.2)$$

$$0 = -\frac{1}{\rho} \frac{\partial p}{\partial y} - g \cos \theta, \quad (2.3)$$

where ρ is the bulk mud density, and g is the acceleration due to gravity. The boundary conditions are

$$u, v = 0 \quad \text{at} \quad y = 0, \tag{2.4}$$

$$p, \tau = 0 \quad \text{at} \quad y = h, \tag{2.5}$$

$$v = \frac{\partial h}{\partial t} + u \frac{\partial h}{\partial x} \quad \text{at} \quad y = h. \tag{2.6}$$

Equations (2.3) and (2.5) indicate that the pressure in the mud flow is approximated as hydrostatic:

$$p = \rho g(h - y) \cos \theta. \tag{2.7}$$

As described in Appendix A (2.1)–(2.7) represent the leading-order results in a perturbation analysis.

For the case of a steady uniform flow, the flow can be divided into a plug layer (unsheared) having velocity $u = U_p$ for $h_s \leq y \leq h_s + h_p = h$ on top of a shear layer in which u increases from zero to U_p as y goes from 0 to h_s , with the yield condition being

$$\tau = \tau_y \quad \text{at} \quad y = h_s. \tag{2.8}$$

Then equations (1.1), (2.2)–(2.5), (2.7), and (2.8) give the following velocity distribution:

$$u = \begin{cases} U_p, & h_s \leq y \leq h \\ U_p [1 - (1 - y/h_s)^{(n+1)/n}], & 0 \leq y \leq h_s \end{cases} \tag{2.9}$$

and the depth-averaged velocity

$$U = h^{-1} \int_0^h u \, dy = U_p \left(1 - \frac{n}{2n+1} \frac{h_s}{h} \right), \tag{2.10}$$

where

$$U_p = \frac{n}{n+1} \left(\frac{\rho g h_s^{n+1} \sin \theta}{\mu_n} \right)^{1/n}. \tag{2.11}$$

Profiles of u/U_p in figure 2 show a plug layer on top of a shear layer, and small values of n seem to have the effect of thickening the plug layer and thinning the shear layer. The bed shear stress is given by

$$\tau_b = \left(\tau_y + \mu_n \left| \frac{n+1}{n} \frac{U_p}{h_s} \right|^n \right) \text{sgn}(U_p). \tag{2.12}$$

It is clear that no flow occurs unless $\tau_p = \rho g h \sin \theta > \tau_y$ for Herschel–Bulkley fluids. Equations (2.9)–(2.12) reduce to those for Bingham-plastic flows when $n = 1$ (Liu & Mei 1989; Jiang & LeBlond 1993; Huang & García 1997 *a, b*), those for power-law fluid flows when $\tau_y = 0$, $h_s = h$, and U_p becomes the velocity at the free surface (Ng & Mei 1994), and those for Newtonian fluid flows when $\tau_y = 0$, $n = 1$, $h_s = h$, and U_p becomes the free-surface velocity (Hunt 1994).

For the case of a gradually varied boundary-layer flow, the well-known von Kármán’s momentum integral method is applied to derive a set of nonlinear partial differential equations that govern the flow. The depth-integrated momentum and continuity equations are obtained in both the shear layer and the plug layer, and the

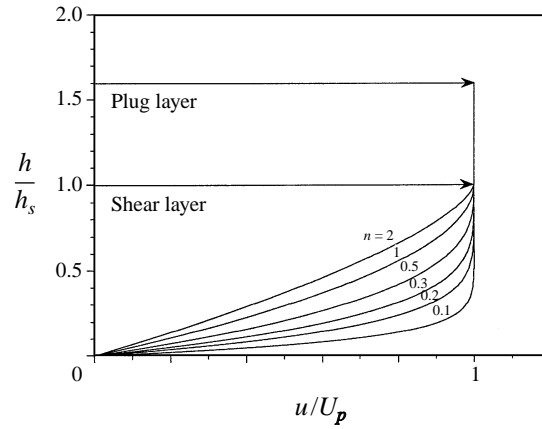


FIGURE 2. Velocity distribution over the cross-section for a uniform flow on a rigid slope, for different values of n . (From Coussot 1994.)

Leibnitz rule is used. Integration of (2.1) with respect to y over the shear layer, i.e. from $y = 0$ to $y = h_s$, gives the interfacial velocity

$$v_i = U_p \frac{\partial h_s}{\partial x} - \alpha_1 \frac{\partial}{\partial x} (U_p h_s). \quad (2.13)$$

Integration of (2.1) with respect to y over the entire flow depth, i.e. from $y = 0$ to h , gives the free-surface velocity

$$v_i = U_p \frac{\partial h}{\partial x} - \frac{\partial q}{\partial x}, \quad (2.14)$$

in which q is the flow rate given by

$$q = \int_0^h u \, dy. \quad (2.15)$$

Substituting the kinematic boundary condition (2.6) into (2.14) yields the depth-integrated continuity equation

$$\frac{\partial h}{\partial t} + \frac{\partial q}{\partial x} = 0. \quad (2.16)$$

Now, integrating (2.2) with respect to y over the shear layer, i.e. from $y = 0$ to h_s , yields

$$\begin{aligned} & \frac{\partial(\alpha_1 U_p h_s)}{\partial t} - U_p \frac{\partial h_s}{\partial t} + \frac{\partial(\alpha_s U_p^2 h_s)}{\partial x} - U_p \frac{\partial(\alpha_1 U_p h_s)}{\partial x} \\ & = \left(-\frac{\partial h}{\partial x} \cos \theta + \sin \theta \right) g h_s + \frac{\tau_y \operatorname{sgn}(U_p) - \tau_b}{\rho}. \end{aligned} \quad (2.17)$$

Integrating (2.2) with respect to y over the plug layer, i.e. from $y = h_s$ to h yields

$$\frac{\partial U_p}{\partial t} + \frac{\partial(U_p^2/2)}{\partial x} = -g \frac{\partial h}{\partial x} \cos \theta + g \sin \theta - \frac{\tau_y \operatorname{sgn}(U_p)}{\rho(h-h_s)}. \quad (2.18)$$

Then, integration of (2.2) with respect to y over the entire flow depth, i.e. from $y = 0$ to h , yields

$$\begin{aligned} \tau_b = \rho \left\{ gh \left(\sin \theta - \frac{\partial h}{\partial x} \cos \theta \right) - \frac{\partial(\alpha_1 U_p h_s)}{\partial t} - \frac{\partial(\alpha_2 U_p^2 h_s)}{\partial x} \right. \\ \left. + U_p \left[\frac{\partial h_s}{\partial t} + \frac{\partial}{\partial x} (\alpha_1 U_p h_s) \right] - (h - h_s) \left[\frac{\partial U_p}{\partial t} + \frac{\partial}{\partial x} \left(\frac{U_p^2}{2} \right) \right] \right\}. \end{aligned} \quad (2.19)$$

From (1.1), $|\tau_b|$ must exceed τ_y for the fluid to flow. In particular, the fluid moves downslope (or upslope) if

$$\tau_b > \tau_y \quad (\text{or } < -\tau_y). \quad (2.20)$$

Whenever $|\tau_b| < \tau_y$, the fluid does not move at all. When $\tau_b = \tau_y$ (or $-\tau_y$), the fluid is at the threshold of downslope (or upslope) flow. Here α_1 and α_2 are shape factors given by, respectively,

$$\alpha_1 = \frac{\int_0^{h_s} u \, dy}{U_p h_s} \quad \text{and} \quad \alpha_2 = \frac{\int_0^{h_s} u^2 \, dy}{U_p^2 h_s}. \quad (2.21)$$

If (2.9) is also true for a transient and non-uniform flow without committing serious errors, except that h and h_s vary with t and x , it is readily obtained that

$$\alpha_1 = \frac{n+1}{2n+1} \quad \text{and} \quad \alpha_2 = \frac{2(n+1)^2}{(2n-1)(3n+2)}, \quad (2.22)$$

which are in the ranges of $0.67 \leq \alpha_1 \leq 1$ and $0.53 \leq \alpha_2 \leq 1$ for $0 \leq n \leq 1$.

Equations (2.16)–(2.20) constitute the governing equations for slender, laminar mud flows following the Herschel–Bulkley model, and they reduce to those for a Bingham model when $n = 1$ (Jiang & LeBlond 1993; Liu & Mei 1994; Huang & García 1997*a*, *b*). A matched-asymptotic perturbation method (Nayfeh 1973) will be employed for their analysis next.

3. Normalization

In fact, not every term in (2.16)–(2.19) has equal significance for the flow under consideration. To investigate the relative magnitude of the terms in these equations, dimensionless variables are introduced by using a number of scales as follows:

$$\left. \begin{aligned} h = h_o h^*, \quad h_s = h_o h_s^*, \quad x = l_o x^*, \quad U_p = u_o U_p^*, \quad t = (l_o/u_o) t^*, \\ \varepsilon = h_o/l_o, \quad \eta = \varepsilon/\tan \theta, \quad \lambda = h_y/h_o, \quad Fr = u_o/(gh_o)^{1/2}, \end{aligned} \right\} \quad (3.1)$$

in which l_o is the length scale in x , h_o the length scale in y , Fr the Froude number, $\varepsilon \ll 1$, u_o the velocity scale given by

$$u_o = \frac{n}{2n+1} \left(\frac{\rho g h_o^{n+1} \sin \theta}{\mu_n} \right)^{1/n}, \quad (3.2)$$

and h_y the yield depth obtained from (2.2) and given by

$$h_y = \tau_y/(\rho g \sin \theta), \quad (3.3)$$

which is the minimum depth for a uniform layer of mud to initiate a flow on a slope. From (2.10), it follows that u_o is the depth-averaged velocity for a steady, uniform power-law fluid flow having a depth h_o .

Introduction of the above variables in (2.16)–(2.20) yields the following dimensionless forms of the approximate governing equations:

$$\left[\frac{\partial h}{\partial t}\right] + \left[\frac{\partial q}{\partial x}\right] = 0, \quad (3.4)$$

$$\begin{aligned} \frac{\eta Fr^2}{\cos \theta} \left\{ \left[\frac{\partial(\alpha_1 U_p h_s)}{\partial t}\right] + \left[\frac{\partial(\alpha_2 U_p^2 h_s)}{\partial x}\right] - \left[U_p \frac{\partial(\alpha_1 U_p h_s)}{\partial x}\right] - \left[U_p \frac{\partial h_s}{\partial t}\right] \right\} \\ = [h_s] - \eta \left[h_s \frac{\partial h}{\partial x}\right] + [\lambda \operatorname{sgn}(U_p)] - [\tau_b], \end{aligned} \quad (3.5)$$

$$\frac{\eta Fr^2}{\cos \theta} \left\{ \left[\frac{\partial U_p}{\partial t}\right] + \left[\frac{\partial}{\partial x} \left(\frac{U_p^2}{2}\right)\right] \right\} = 1 - \eta \left[\frac{\partial h}{\partial x}\right] - \left[\frac{\lambda \operatorname{sgn}(U_p)}{h - h_s}\right], \quad (3.6)$$

$$\left| [h] - \eta \left[h \frac{\partial h}{\partial x}\right] - \frac{\eta Fr^2}{\cos \theta} (C + D) \right| > \lambda, \quad (3.7)$$

where

$$C = \left[\frac{\partial(\alpha_1 U_p h_s)}{\partial t}\right] + \left[\frac{\partial(\alpha_2 U_p^2 h_s)}{\partial x}\right] - \left[U_p \frac{\partial h_s}{\partial t}\right] - \left[U_p \frac{\partial(\alpha_1 U_p h_s)}{\partial x}\right], \quad (3.8)$$

$$D = \left[(h - h_s) \frac{\partial U_p}{\partial t}\right] + \left[(h - h_s) \frac{\partial}{\partial x} \left(\frac{U_p^2}{2}\right)\right], \quad (3.9)$$

and τ_b^* is the normalized value given by

$$\tau_b = \tau_b^* \rho g h_o \sin \theta. \quad (3.10)$$

The asterisk superscript has been omitted in (3.4)–(3.9) for notational convenience. The Reynolds number effects in (3.5)–(3.7) can be discovered by defining the Reynolds number Re as

$$Re = \rho u_o^{2-n} h_o^n / \mu_n, \quad (3.11)$$

which indicates, with the help of (3.1) and (3.2), that

$$\frac{Fr^2}{Re \sin \theta} = \left(\frac{n}{2n+1}\right)^n \sim O(1) \quad (3.12)$$

since $0.33 \leq [n/(2n+1)]^n < 1$ for $0 < n \leq 1$.

4. Matched-asymptotic analysis

4.1. Outer solution

The slope is assumed to be steep enough so that the conditions

$$\eta \ll 1 \quad \text{and} \quad \tan \theta \leq O(1) \quad (4.1a)$$

are easily satisfied. Both l_o and h_o have been selected so that all the terms in the square brackets of (3.4)–(3.9) are of $O(1)$. Thus, if

$$Fr^2 \leq O(\cos \theta) \quad \text{and} \quad Re \leq O(1/\tan \theta), \quad (4.1b)$$

then (3.4)–(3.7) reduce to the kinematic-wave approximation (Choi & García 1993)

$$\frac{\partial h^*}{\partial t^*} + \frac{\partial u}{\partial x^*} \left[U_p^* \left(h^* - \frac{n}{2n+1} h_s^* \right) \right] = 0, \tag{4.2}$$

$$U_p^* = \frac{2n+1}{n+1} h_s^{*(n+1)/n}, \tag{4.3}$$

$$h^* - h_s^* = \lambda \operatorname{sgn}(U_p), \tag{4.4}$$

$$h^* > \lambda, \tag{4.5}$$

in which (2.9) and (2.22) are used, U_p^* is the dimensionless velocity in the plug layer, and $\operatorname{sgn}(U_p) = 1$ since the flow moves in the direction of the positive x -axis. Substituting (4.3) and (4.4) into (2.10) gives the dimensionless averaged velocity over the entire flow depth as

$$U^* = (h^* - \lambda)^{(n+1)/n} \left(1 + \frac{n}{n+1} \frac{\lambda}{h^*} \right). \tag{4.6}$$

Substitution of (4.3) and (4.4) into (4.2) yields

$$\frac{\partial h^*}{\partial t^*} + \frac{2n+1}{n} h^* (h^* - \lambda)^{1/n} \frac{\partial h^*}{\partial x^*} = 0, \tag{4.7}$$

where h^* is the only unknown and (4.5) is satisfied. Equations (4.3) and (4.4) then give approximate expressions for U_p^* and h_s^* . With the help of the chain rule, (4.7) can be changed into two ordinary differential equations, such that

$$\frac{dh^*}{dt^*} = 0 \tag{4.8}$$

along characteristic curves

$$\frac{dx^*}{dt^*} = \frac{2n+1}{n} h^* (h^* - \lambda)^{1/n} \tag{4.9}$$

in the (x^*, t^*) -plane. Equation (4.8) indicates that h^* is constant along characteristic curves, and (4.9) indicates that the characteristic curves are all straight lines with slopes determined by the particular value of h^* on each characteristic curve.

If the flow is assumed to be released from a point source† at $x^* = t^* = 0$, then all of the characteristic curves with non-zero values of h^* pass through this point in the (x^*, t^*) -plane. Thus, (4.9) gives

$$x^* = \frac{2n+1}{n} h^* (h^* - \lambda)^{1/n} t^*. \tag{4.10}$$

Note that at the origin $h^* = \lambda$. The location of a wave front at the leading edge of the flow can be found by requiring that the area of material in a vertical plane remains

† The point source is explained as follows. If initially $h^* = f(x^*)$, the characteristics is given by $x^* = x_0^* + (2n+1)f(x_0^*)[f(x_0^*) - \lambda]^{1/n}/n$ where x_0^* is the initial value of the characteristic. The solution of (4.9) is then given by $x^* = x_0^* + (2n+1)h^*[h^* - \lambda]^{1/n}t^*/n$. For $x^* = x_0^*$, this solution can be approximated by $x^* = (2n+1)h^*[h^* - \lambda]^{1/n}t^*/n$.

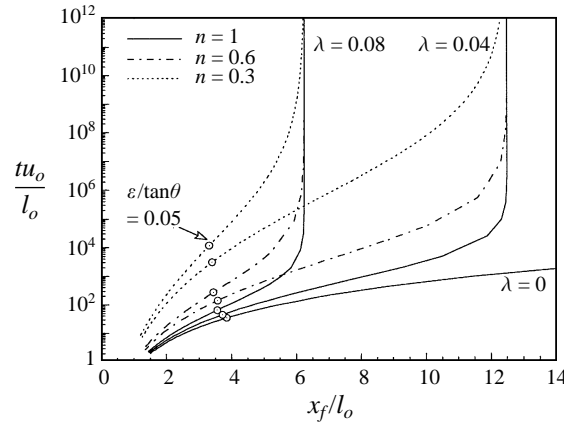


FIGURE 3. Kinematic-wave shock coordinate plotted as function of time for flows from a point source. $A^* = 0.5$.

constant with time (Whitham 1974). Thus, if the wave front location is $x^* = x_f^*(t)$, this requires

$$A^* = \int_0^{x_f^*(t^*)} h^* dx^* \quad (4.11)$$

in which t^* is a parameter, and the constant dimensionless area, A^* , is normalized as

$$A^* = A/(l_o h_o). \quad (4.12)$$

Integrating (4.11) by changing the integrating variable with the help of (4.10), yields an implicit form for the front depth h_f^* at different times as follows:

$$A^* = \int_0^{h_f^*} h^* \frac{dx^*}{dh^*} dh^* = (h_f^* - \lambda)^{1/n} \left(\frac{n+1}{n} h_f^{*2} + \frac{1}{n+1} h_f^* \lambda + \frac{n}{n+1} \lambda^2 \right) t^*. \quad (4.13)$$

Setting $x^* = x_f^*$ and $h^* = h_f^*$ in (4.10) and eliminating t^* from the resulting equation and (4.13), gives the front location

$$x_f^* = \frac{2n+1}{n} \left(\frac{n+1}{n} h_f^* + \frac{1}{n+1} \lambda + \frac{n}{n+1} \frac{\lambda^2}{h_f^*} \right)^{-1} A^* \quad (4.14)$$

as an explicit function of the flow depth just upstream from the wave front, h_f^* . For a given front coordinate, flow depths at different locations can be also obtained from (4.10) by

$$\frac{x^*}{x_f^*} = \frac{h^*(h^* - \lambda)^{1/n}}{h_f^*(h_f^* - \lambda)^{1/n}}. \quad (4.15)$$

Finally, differentiating (4.10) and (4.13) with respect to t^* and eliminating dh_f^*/dt^* from the resulting equations gives the propagation velocity of the wave front as

$$\frac{dx_f^*}{dt^*} = (h_f^* - \lambda)^{(n+1)/n} \left(1 + \frac{n}{n+1} \frac{\lambda}{h_f^*} \right). \quad (4.16)$$

Comparison of (4.6) and (4.16) indicates that the wave front propagates at the same velocity as that of the fluid just upstream from it.

Equations (4.11), (4.14), and (4.16) show that a Herschel–Bulkley flow originated from a constant-volume source only propagates a finite distance downslope, with x_f^* asymptotically approaching A^*/λ (figure 3), h^* asymptotically approaching λ (figure

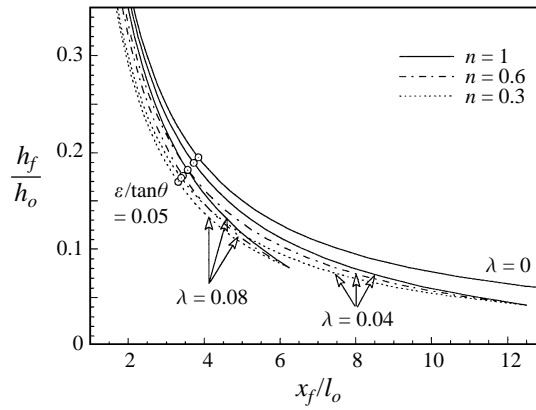


FIGURE 4. Kinematic-wave shock depth plotted as function of shock coordinate for flows from a point source. $A^* = 0.5$.

4), and U_f^* asymptotically falling to zero (figure 5). The final stage of the flow is similar to a creeping motion. The smaller the value of λ , the faster the flow will move downslope, and the more rapidly both the front depth and the front velocity will decay with time. The small value of n has no effect on the runout extent, but greatly slows down the flow and the decay of both the front depth and the front velocity. The hydrographs for Bingham ($\lambda = 0.04, n = 1$), Newtonian ($\lambda = 0, n = 1$), and Herschel–Bulkley ($\lambda = 0.04, n = 0.4$) fluid flows at the gauging station with $x/L = 5.5$ are plotted in figure 6. The hydrograph for the Herschel–Bulkley flow is seen to have a slower, lower, and wider flood peak, and the decline of the peak is more gentle than in the other two cases.

The solution given by (4.10) and (4.13)–(4.16) is a relatively simple result that has been obtained by considering a Herschel–Bulkley fluid released from a point source. To see the solution for a source of finite size, as an example, a dam-burst or mud-slide problem with an initial triangular shape on a slope is considered next. It is assumed that the sediment movement which results in the mud-slide behaving like a Herschel–Bulkley fluid flow is homogeneous and instantaneous, that the mud mass in the slide remains constant with time, and that the lateral length scale is many times larger than the flow depth. By introducing the scales

$$l_o = L \quad \text{and} \quad h_o = H, \tag{4.17}$$

where L and H are the maximum length and height of the initial sediment mass, respectively, then the initial condition that is required for integration of (4.8) and (4.9) is given by

$$h^*(x^*, 0) = \begin{cases} x^*, & 0 \leq x^* \leq 1 \\ 0, & -\infty < x^* < 0 \quad \text{or} \quad 1 < x^* < \infty. \end{cases} \tag{4.18}$$

Integrating (4.8) and (4.9) with the help of (4.18) and (4.5) gives

$$x^* = \frac{2n+1}{n} h^*(h^* - \lambda)^{1/n} t^* + h^*, \tag{4.19}$$

which holds in the (x^*, t^*) -plane only, within a region covered by characteristic curves that leave the x -axis along the interval $\lambda \leq x^* \leq 1$. To prevent characteristic curves leaving the x -axis for $x^* > 1$ from crossing characteristic curves leaving the x -axis for

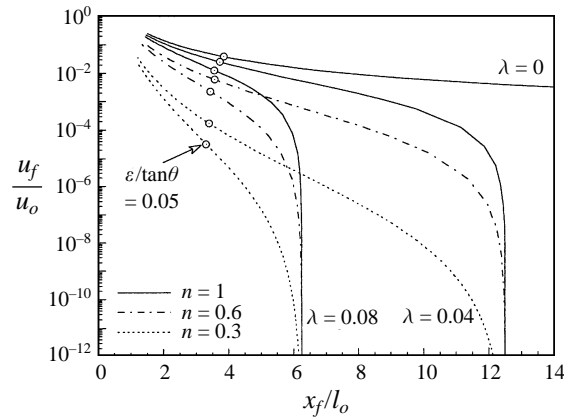


FIGURE 5. Kinematic-wave shock velocity plotted as function of shock coordinate for flows from a point source. $A^* = 0.5$.

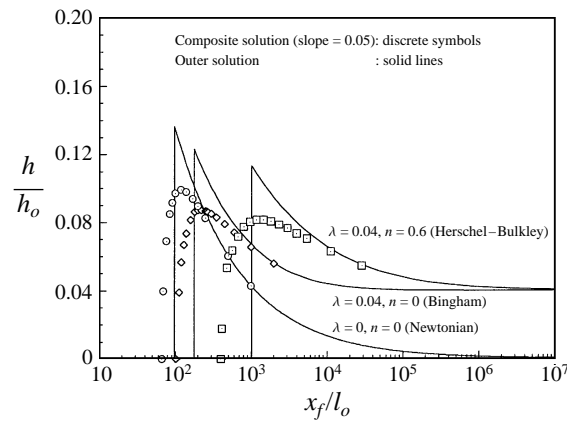


FIGURE 6. Hydrograph at $x/l_o = 5.5$ from a point source of $A^* = 0.5$.

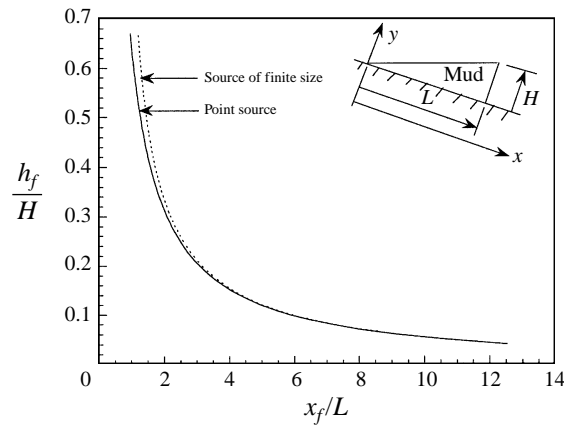


FIGURE 7. Comparison of kinematic-wave shock depths for mud flows from a point source and a source of finite size. $A^* = 0.5$, $\lambda = 0.04$, $n = 0.4$.

$\lambda \leq x^* \leq 1$, the front location is fixed by using mass conservation requirement, which is similar to (4.11) and given by

$$A^* = \int_{\lambda}^{x_f^*} h^* dx^*, \tag{4.20}$$

where x_f^* is the front coordinate, and A^* is given by

$$A^* = (1 - \lambda^2)/2. \tag{4.21}$$

Integrating (4.20) by changing the integrating variable with the help of (4.19) yields an implicit form for the flow depth just upstream from the wave front, h_f^* , at different times,

$$t^* = \frac{(1 - h_f^{*2})/2}{\left(\frac{n+1}{n} h_f^{*2} + \frac{1}{n+1} h_f^* \lambda + \frac{n}{n+1} \lambda^2\right) (h - \lambda)^{1/n}}. \tag{4.22}$$

The relation between the front coordinate x_f^* and h_f^* can be obtained from (4.19) and (4.22) as

$$x_f^* = \frac{\left(\frac{2n+1}{2n} + \frac{1}{2n} h_f^{*2} + \frac{1}{n+1} h_f^* \lambda + \frac{n}{n+1} \lambda^2\right) h_f^*}{\frac{n+1}{n} h_f^{*2} + \frac{1}{n+1} h_f^* \lambda + \frac{n}{n+1} \lambda^2}. \tag{4.23}$$

A plot of (4.14) and (4.23) is shown in figure 7 for $\lambda = 0.04$ and $n = 0.4$. Further numerical inspection indicates that for $\lambda \leq 0.1$ and $0.1 \leq n \leq 1$, the two solutions for the front depth, h_f^* , differ by less than 2% at $x_f^* = 5$ and become even closer farther downstream. The wave front of the mud flow caused by the mud-slide is seen to propagate $\lambda/2$ farther downslope than that from a point source. This corresponds to a dimensional distance of $\lambda L/2$. This is due to the fact that the fluid mass in the region $0 < x^* < \lambda$, whose depth is defined by (4.10) for the flow from a point source, is $\lambda^2 LH/2$ by volume larger than that in the same region in the mud-slide, which is actually still and has a depth of xH/L . Such an artificial difference can be prevented by moving the point source coordinate to $\lambda/2$. Thus, two significant points can be made from the similarity of the two solutions. First, since the solutions for the point and distributed sources are virtually identical for $x_f^* > 5$, there seems to be no practical reason to use the more complicated solution for a distributed source after this point. Secondly, since the kinematic-wave solution is independent asymptotically only on the initially movable mass of fluid and not on the initial distribution of fluid mass, it appears likely that an exact solution of (2.16)–(2.20) may also have an asymptotic behaviour that has no memory of the past history of the flow. In other words, the perturbation solution of (2.16)–(2.20) is asymptotically valid even though this solution yields poor approximations for early time stages (Huppert 1982*a*).

4.2. Validity

As indicated previously in the scaling process, the kinematic-wave solution is asymptotically valid only when (4.1*a*) is satisfied. If the length scales are chosen as $l_o = x_f$ and $h_o = h_f$ for convenience, then (4.23) can be rewritten as

$$\eta = \frac{\frac{n+1}{n} h_f^2 + \frac{1}{n+1} h_f h_y + \frac{n}{n+1} h_y^2}{\frac{2n+1}{2n} H^2 + \frac{1}{2n} h_f^2 + \frac{1}{n+1} h_f h_y + \frac{n}{n+1} h_y^2}. \tag{4.24}$$

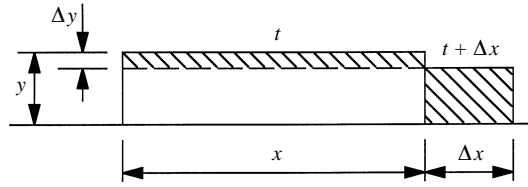


FIGURE 8. Conceptual motion of a boundary-layer flow with a front.

Now the perturbation solution is assumed to be valid when $\varepsilon/\tan\theta \leq 0.05$, and the validity boundary (i.e. $\varepsilon/\tan\theta = 0.05$) has been plotted as circle-dot symbols in figures 3–5. Thus, the perturbation solution developed herein would provide an accurate approximation of the physical problem for values of x_f/l_o that lie to the right of the circle-dot symbols in figures 3–5. In particular, the solution for $\lambda = 0$ and $n = 1$ (Newtonian) becomes valid after the front passes the point $x_f/l_o = 3.9$, the solution for $\lambda = 0.08$ and $n = 1$ (Bingham) becomes valid after the front passes the point $x_f/l_o = 3.6$, and the solution for $\lambda = 0.08$ and $n = 0.1$ (Herschel–Bulkley) becomes valid after the front passes the point $x_f/l_o = 3.2$. Non-zero values of λ and small values of n ($0 < n \leq 1$) seem to move upstream the point at which the perturbation solution becomes valid. Since all the terms in the square brackets of (3.4)–(3.9) are of $O(1)$, the neglected terms in (3.4)–(3.7) are approximately within 5% of the remaining terms. Therefore, the kinematic-wave solution is relatively accurate since, from perturbation theory, the second-order solution is within 5% of the first-order solution.

4.3. Inner solution

The solution given by (4.10) and (4.13)–(4.16) is the first-order outer approximation in a singular perturbation expansion. This solution gives accurate results for the spreading rate of low-Reynolds-number flows and the free-surface profile away from the wave front, having an $O(\varepsilon/\tan\theta)$ error after the wave front has advanced a distance h_f/ε downstream. However, the free-surface profile is excessively simplified near the wave front, where the kinematic-wave approximation is not sufficient, since $\partial h/\partial x$ is not small any more, and (3.4)–(3.7) have been scaled incorrectly.

It is noted that, after a certain distance downstream, the wave front depth varies slowly both in time and along the downstream direction, implying that the wave front is a quasi-permanent wave moving at a nearly constant velocity. This boundary condition (meaning ‘those that specify the agency generating the motion of the fluid as remarked by Batchelor 1967) indicates that the components in the x -direction are still larger than those in the y -direction as seen in

$$\frac{dh_f}{dt} \sim \varepsilon \frac{dx_f}{dt} \quad \text{and} \quad \frac{d^2h_f}{dt^2} \sim \varepsilon \frac{d^2x_f}{dt^2}. \quad (4.25)$$

Mathematically, this can be proved as follows. Shown in figure 8 is a conceptual motion of a boundary-layer flow in an infinitesimal time duration Δt . By mass conservation, the two cross-hatched areas should be equal, i.e.

$$(y - \Delta y) \Delta x = x \Delta y. \quad (4.26)$$

Neglecting the high-order small term $\Delta x \Delta y$, (4.26) gives

$$\frac{\Delta y}{\Delta x} = \frac{y}{x} = O(\varepsilon) \quad 1. \quad (4.27)$$

By taking the limit $\Delta t \rightarrow 0$, it is obtained that

$$\frac{v}{u} = \lim_{\Delta t \rightarrow 0} \frac{\Delta y / \Delta t}{\Delta x / \Delta t} = \frac{y}{x} = O(\varepsilon) \quad 1, \quad (4.28)$$

$$\frac{dv/dt}{du/dt} = \lim_{\Delta t \rightarrow 0} \frac{\Delta v / \Delta t}{\Delta u / \Delta t} = \frac{y}{x} = O(\varepsilon) \quad 1. \quad (4.29)$$

By taking a leading-order view of the motion, the wave front is a quasi-permanent wave. Equations (4.27)–(4.29) indicate that the physical scaling for the flow near the wave front is similar to that for the flow far away from the wave front as described in Appendix A, the only exception being the pressure-gradient term which becomes important. Therefore, equations (2.1)–(2.3) are still valuable near the wave front. On the other hand, if $O(x) \sim O(y)$, the motions in both x - and y -directions are important. In lubrication theory, equations (2.1)–(2.3) have been useful approximations near the wave front, with the inertia terms being neglected (Huppert 1982*b*; Liu & Mei 1989) when the Reynolds number is low and surface tension is negligible.

In the following, therefore, a set of inner variables is proposed to rescale (3.4)–(3.7):

$$\xi^* = (x^* - x_f^*) / \eta, \quad (4.30a)$$

$$h^* = h_i^*, \quad h_s^* = h_{si}^*, \quad U^* = U_i^*, \quad U_p^* = U_{pi}^*, \quad t^* = t_i^*, \quad \tau_b^* = \tau_{bi}^* \quad (4.30b)$$

in a way similar to that proposed by Hunt (1994) for Newtonian-fluid debris flows. Then, (3.4)–(3.9) become, with the asterisk superscript omitted for notational convenience,

$$\left[\frac{\partial}{\partial \xi} \left(h_i \left\langle U_i - \frac{dx_f}{dt} \right\rangle \right) \right] + \eta \left[\frac{\partial h_i}{\partial t_i} \right] = 0, \quad (4.31)$$

$$\begin{aligned} \frac{Fr^2}{\cos \theta} \left\{ \eta \left[\frac{\partial (\alpha_1 U_{pi} h_{si})}{\partial t_i} \right] - \eta \left[U_{pi} \frac{\partial h_{si}}{\partial t_i} \right] + \left[\frac{\partial}{\partial \xi} \left(\frac{\alpha_2 U_{pi}^2 h_{si}}{U_i} \left\langle U_i - \frac{dx_f}{dt} \right\rangle \right) \right] \right. \\ \left. - \left[U_{pi} \frac{\partial}{\partial \xi} \left(\frac{\alpha_1 U_{pi} h_{si}}{U_i} \left\langle U_i - \frac{dx_f}{dt} \right\rangle \right) \right] \right\} = [h_{si}] - \left[h_{si} \frac{\partial h_i}{\partial \xi} \right] + [\lambda \operatorname{sgn}(U_{pi})] - \tau_{bi}, \quad (4.32) \end{aligned}$$

$$\frac{Fr^2}{\cos \theta} \left\{ \eta \left[\frac{\partial U_{pi}}{\partial t_i} \right] + \left[\frac{\partial}{\partial \xi} \left(\frac{U_{pi}^2}{2U_i} \left\langle U_i - \frac{dx_f}{dt} \right\rangle \right) \right] \right\} = 1 - \left[\frac{\partial h_i}{\partial \xi} \right] - \left[\frac{\lambda \operatorname{sgn}(U_{pi})}{h_i - h_{si}} \right], \quad (4.33)$$

and

$$\left| [h_i] - \left[h_i \frac{\partial h_i}{\partial \xi} \right] - \frac{Fr^2}{\cos \theta} (C' + D') \right| > \lambda \quad (4.34)$$

where

$$\begin{aligned} C' = \eta \left[\frac{\partial (\alpha_1 U_{pi} h_{si})}{\partial t_i} \right] - \eta \left[U_{pi} \frac{\partial h_{si}}{\partial t_i} \right] + \left[\frac{\partial}{\partial \xi} \left(\frac{\alpha_2 U_{pi}^2 h_{si}}{U_i} \left\langle U_i - \frac{dx_f}{dt} \right\rangle \right) \right] \\ - \left[U_{pi} \frac{\partial}{\partial \xi} \left(\frac{\alpha_1 U_{pi} h_{si}}{U_i} \left\langle U_i - \frac{dx_f}{dt} \right\rangle \right) \right], \quad (4.35) \end{aligned}$$

$$D' = \eta \left[(h_i - h_{si}) \frac{\partial U_{pi}}{\partial t_i} \right] + \left[(h_i - h_{si}) \frac{\partial}{\partial \xi} \left(\frac{U_{pi}^2}{2U_i} \left\langle U_i - \frac{dx_f}{dt} \right\rangle \right) \right]. \quad (4.36)$$

The derivation of (4.31) is given in Appendix B. Applying (4.1a) in (4.31) and integrating yields

$$h_i^* \left(U_i^* - \frac{dx_f^*}{dt^*} \right) = f(t_i^*), \quad (4.37)$$

where $f(t_i^*)$ is a function of t_i^* only. The boundary condition that h_i^* vanishes at the leading edge of the wave front for all values of t_i^* renders $f(t_i^*) = 0$. Hence,

$$U_i^* = \frac{dx_f^*}{dt^*}, \quad (4.38)$$

which shows that velocities near the wave front change only with time. Then, applying (4.1) and (4.38) in (4.32)–(4.34) yields

$$h_{si}^* \frac{\partial h_i^*}{\partial \xi^*} = h_{si}^* + \lambda \operatorname{sgn}(U_p) - \tau_{bi}^*, \quad (4.39)$$

$$(h_i^* - h_{si}^*) \frac{\partial h_i^*}{\partial \xi^*} = h_i^* - h_{si}^* - \lambda \operatorname{sgn}(U_{pi}), \quad (4.40)$$

$$\left| h_i^* - h_{si}^* \frac{\partial h_i^*}{\partial \xi^*} \right| > \lambda. \quad (4.41)$$

It is noted that the inertia terms are neglected due to the fact that $\eta = 1$ and $U_i^* - dx_f^*/dt^* = 0$. For the problem under consideration, since the flow moves in the direction of the positive x -axis, $\operatorname{sgn}(U_p) = 1$ near the wave front. Obviously, the condition (4.41) is satisfied. Then adding (4.39) and (4.40) gives

$$h_i^* - h_{si}^* \frac{\partial h_i^*}{\partial \xi^*} = \tau_{bi}^* \quad (4.42)$$

which can be solved for h_i^* under some boundary condition if the basal shear stress τ_{bi}^* is known. A direct way is to solve (2.12), (4.40), and (4.42) for values of $h_i^*(\xi)$ and $h_{si}^*(\xi)$, and details along these lines are shown in Huang & García (1997b). However, a rigorous way is used herein, in which the basal shear stress in a non-uniform flow having a depth of h_i^* is derived. As shown in Appendix C, the basal shear stress near the wave front is given by

$$\tau_{bi}^* = \lambda + \left[\frac{(n+1) h_i^* U_i^*}{(2n+1) h_i^* h_{si}^* - n h_{si}^{*2}} \right]^n, \quad (4.43)$$

where U_i^* is given by (4.38), and h_{si}^* can be solved by (4.40). Therefore, it can be shown that

$$\left(\frac{h_i^* \phi^* - \lambda}{h_f^* - \lambda} \right)^{(n+1)/n} = \frac{\left(1 - \frac{n}{2n+1} \frac{h_f^* - \lambda}{h_f^*} \right) \phi^*}{\left(1 - \frac{n}{2n+1} \frac{h_i^* - \lambda/\phi^*}{h_i^*} \right)} \quad (4.44)$$

where $\phi^* = 1 - \partial h_i^*/\partial \xi^*$. Equation (4.44) has only one unknown, h_i^* , and can be easily solved for some boundary condition. Numerical inspection of (4.44) shows that $h_i^* \rightarrow h_f^*$ as $\xi^* \rightarrow -\infty$. This indicates that the inner solution matches the outer solution correctly, i.e.

$$\lim_{x^* - x_f^* \rightarrow 0} h_i^* = \lim_{\xi^* \rightarrow -\infty} h_i^* = h_f^*. \quad (4.45)$$

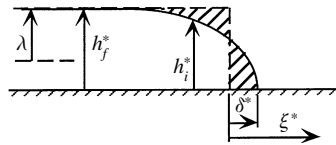


FIGURE 9. Inner solution near the shock front.

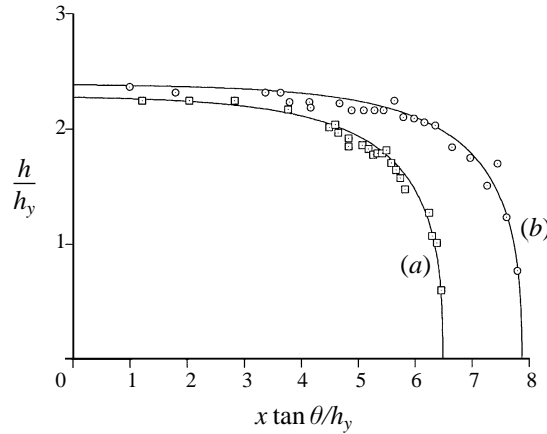


FIGURE 10. Comparison of inner solution with experimental results obtained by Liu & Mei (1989).

The boundary condition required for solving (4.44) is the mass conservation requirement (Whitham 1975), which can be written in the form

$$\int_{-\infty}^0 (h_f^* - h_i^*) d\xi^* = \int_0^{\delta^*} h_i^* d\xi^*, \tag{4.46}$$

where δ^* is defined in figure 9 as the distance between the kinematic-wave front and the front nose in the inner solution. This requires that the two cross-hatched areas in figure 9 be equal.

When $h_f^* = \lambda$, (4.44) can be integrated to yield

$$(\xi^* + \text{constant}) \tan \theta = h_i^* + \lambda \ln |h_i^* - \lambda| \tag{4.47}$$

which gives the depth of a three-dimensional mud-flow deposit along its centreline on an inclined plane (Coussot *et al.* 1996) or the depth of a two-dimensional mud flow at the threshold condition for motion downslope (Liu & Mei 1989). The constant in (4.47) is determined by (4.46). When $h_f^* > \lambda$, the inner solution describes a two-dimensional permanent gravity wave which spreads at a speed determined by (4.38) and has a free-surface profile determined by (4.44) (Liu & Mei 1989). The free-surface profiles computed from (4.44) are seen to agree very well with experimental results obtained by Liu & Mei (1989) in figure 10. The mud they used had the following properties: $\rho = 1.106 \text{ g cm}^{-3}$, $\tau_y = 8.75 \text{ dyne cm}^{-2}$, $n = 1$, and $\mu_1 = 0.34 \text{ g cm}^{-1} \text{ s}^{-1}$. The experimental conditions are: (a) $\theta = 1.47^\circ$, $U_i = 5.22 \text{ cm s}^{-1}$, $h_f = 0.71 \text{ cm}$, $h_y = 0.31 \text{ cm}$, and $Re = 0.63$; (b) $\theta = 0.90^\circ$, $U_i = 9.46 \text{ cm s}^{-1}$, $h_f = 1.22 \text{ cm}$, $h_y = 0.51 \text{ cm}$, and $Re = 3.55$.

4.4. Composite solution

The outer and inner solutions obtained in (4.10), (4.13)–(4.16), (4.44), and (4.46) are in dimensionless form scaled by the variables in (3.1) and (4.30), and their validity is restricted by (4.1). Thus, it is inconvenient to use these dimensionless solutions for

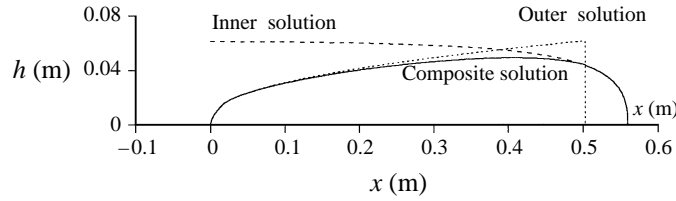


FIGURE 11. Composite solution.

interpretation and numerical computations. This can be readily avoided by expressing the inner and outer solutions in dimensional variables and noting that the length scales l_o and h_o cancel out in the final result. The outer solution is then given by

$$x = [\rho g h^n (h - h_y) \sin \theta / \mu_n]^{1/n} t, \quad (4.48)$$

$$A = \frac{n}{2n+1} \left[\frac{\rho g (h_f - h_y) \sin \theta}{\mu_n} \right]^{1/n} \left(\frac{n+1}{n} h_f^2 + \frac{1}{n+1} h_f h_y + \frac{n}{n+1} h_y^2 \right) t, \quad (4.49)$$

$$x_f = \frac{2n+1}{n} \left(\frac{n+1}{n} h_f + \frac{1}{n+1} h_y + \frac{n}{n+1} \frac{h_y^2}{h_f} \right)^{-1} A, \quad (4.50)$$

$$\frac{x}{x_f} = \frac{h(h - h_y)^{1/n}}{h_f(h_f - h_y)^{1/n}}, \quad (4.51)$$

$$\frac{dx_f}{dt} = \frac{n}{2n+1} \left[\frac{\rho g (h_f - h_y)^{n+1} \sin \theta}{\mu_n} \right]^{1/n} \left(1 + \frac{n}{n+1} \frac{h_y}{h_f} \right), \quad (4.52)$$

while the inner solution takes the form

$$\left(\frac{h_i \phi - h_y}{h_f - h_y} \right)^{(n+1)/n} = \frac{\left(1 - \frac{n}{2n+1} \frac{h_f - h_y}{h_f} \right) \phi}{\left(1 - \frac{n}{2n+1} \frac{h_i - h_y / \phi}{h_i} \right)} \quad (4.53)$$

with the boundary condition given by

$$\int_{-\infty}^0 (h_f - h_i) d\xi = \int_0^\delta h_i d\xi, \quad (4.54)$$

where $\phi = 1 - (dh_i/d\xi)/\tan \theta$, and $\xi = x - x_f$. Thus, a composite solution, h_c , can be obtained by adding the inner and outer solutions and subtracting their common matching term, h_f , as follows:

$$h_c = h + h_i - h_f + O(\varepsilon/\tan \theta). \quad (4.55)$$

The composite solutions are also plotted in figure 6, and should give more reasonable descriptions of the physical problem than the outer solutions. Composite velocities are obtained from (4.6) with h from (4.48) or (4.51). As shown by a computed result in figure 11, the composite solution is as good an approximation in the outer region as the outer solution, and it is as good an approximation in the inner region as the inner solution. The validity of the composite solution uniformly over the whole runout distance at this time is achieved through an overlapping region, hence there is no gap between the two regions. The size of the inner region is characterized by the inner scaling analysis and given by

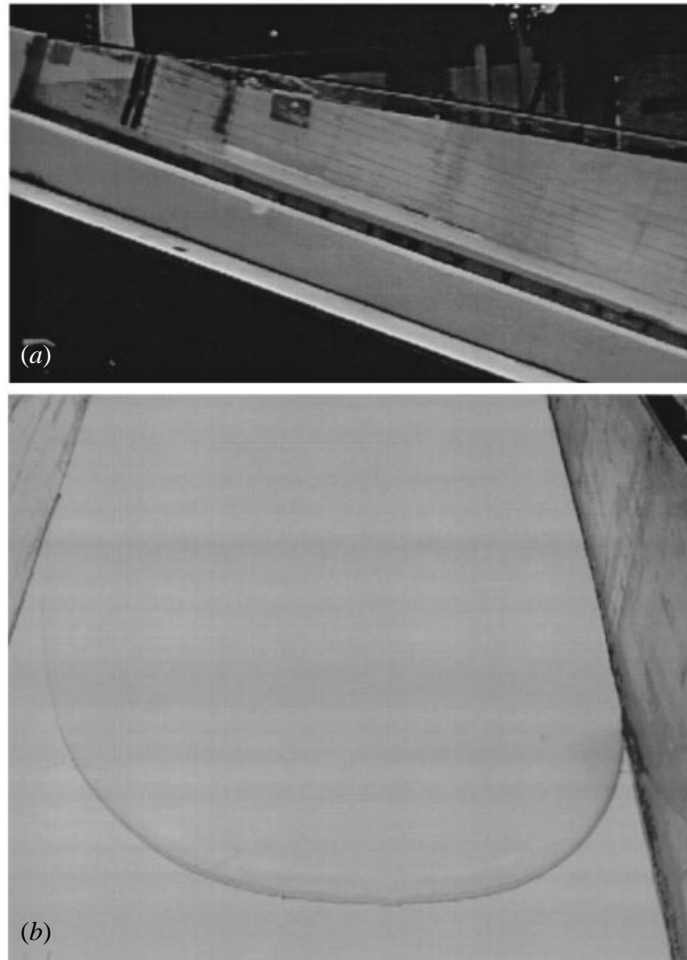


FIGURE 12. (a) Lateral view of Plexiglas tank used in the experiments, (b) mudflow front.

Cases	C_v (%)	Bulk density, ρ (g cm ⁻³)	τ_y (N m ⁻²)	μ_n (N m ⁻² s ⁿ)	n
(1)	22.13	1.365	17.86	21.30	0.24
(2)	21.07	1.348	14.10	10.20	0.34
(3)	19.59	1.323	9.96	7.10	0.38
(4)	17.11	1.282	6.40	6.40	0.29
(5)	14.24	1.235	2.91	1.70	0.36
(6)	13.05	1.215	2.21	0.22	0.75

TABLE 2. Rheological measurements for kaolinite suspensions

or dimensionally as
$$x^* - x_f^* = O(-1) \tag{4.56 a}$$

$$x - x_f = O(-x_f) \tag{4.56 b}$$

if $h_o = h_f$ and $l_o = x_f$ are selected. The size of the overlapping region is characterized by the matching (4.45) as

$$x^* = O(1) \tag{4.57 a}$$

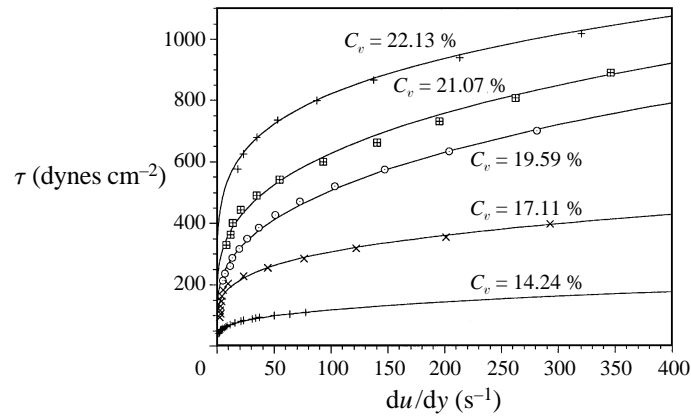


FIGURE 13. Rheological measurements for kaolinite suspensions. (See table 2 for parameters).

or dimensionally as

$$x = O(x_f) \quad (4.57b)$$

if $h_o = h_f$ and $l_o = x_f$ are selected.

Note that the composite solution in (4.55) increases suddenly from zero to the yield depth at the upstream end of the flow. For flows without a retaining wall on the upstream side, such a free-surface profile near the tail is not realistic. The mud near the tail is in fact at the threshold condition after it just stops moving in the upstream direction. Thus, the free-surface profile near the tail is governed by (4.39) and (4.40) in which $U_p = 0$ and $\text{sgn}(U_p) = -1$. These two equations then give the following differential equation:

$$h_i \frac{\partial h_i}{\partial \xi} = (h_i + h_y) \tan \theta \quad (4.58)$$

in which $\xi = x$. The fluid depth increases from zero to the yield depth near the tail as described by (4.58).

4.5. Experiments

A set of laboratory experiments to check the theoretical model was conducted. The experiments were carried out in a tilted Plexiglas tank (figure 12), which is 30 cm wide, 100 cm long, and 6 cm and 22 cm deep at the upstream and downstream ends, respectively. A 10 cm long reservoir is located at the upstream end, behind a sliding gate. Kaolinite was well mixed with tap water by using a blender, then the suspension was poured into the reservoir. A mud sample was taken, after each experiment, to a Bohlin constant-stress rheometer to measure its rheological properties at the experimental temperature. With a certain volume of mud suspension in the reservoir, a mud flow was generated by suddenly pulling out the gate. A digital video camera was used to capture the spreading flow from above at a rate of 30 frames per second. The rate of spreading was obtained with the help of a $1 \times 1 \text{ cm}^2$ grid system marked on the bottom of the tank. A laser displacement sensor was mounted above the tank to obtain hydrographs at a certain gauging station. Free-surface profiles were recorded for slow flows by placing a thin stainless steel ruler along the centreline into the mud flow and pulling the ruler out quickly. This was performed manually and took about 0.1 s.

In the experiments, the Herschel–Bulkley model was found to give the best fit to all rheological measurements as shown in figure 13 and table 2. The yield stress was obtained by extrapolating the experimental shear stress–shear rate data at zero rate of

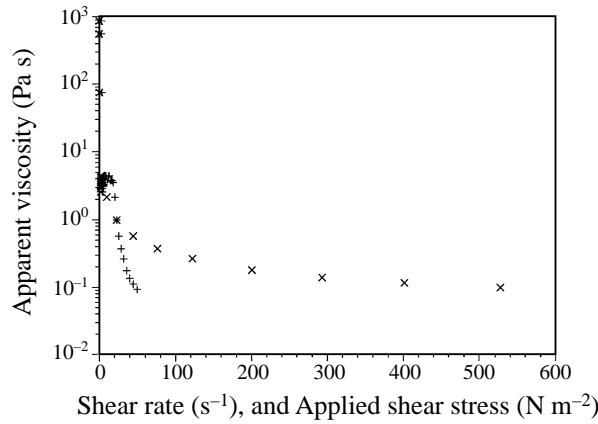


FIGURE 14. Measured apparent viscosity varying with rate of shear (\times) and applied shear stress ($+$). Yield stress is that below which the apparent viscosity tends to infinity.

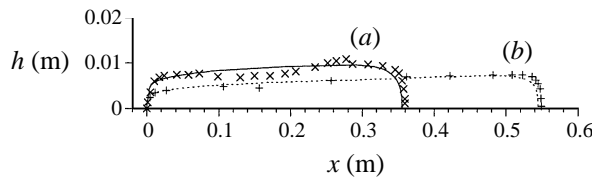


FIGURE 15. Comparison of computed (—, --) and measured (+, \times) free-surface profiles. (Experimental condition can be found in the text.)

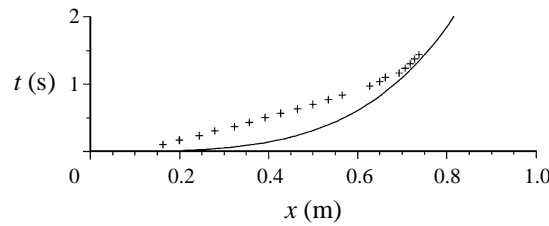


FIGURE 16. Comparison of computed (—) and measured (+) spreading relation. (Experimental condition can be found in the text.)

shear. The extrapolated yield stress can be checked by a logarithmic plot of the apparent viscosity and shear stress or rate of shear, in which the yield stress is found as the lower stress limit at which the apparent viscosity tends to infinity (figure 14).

With measured values of τ_y , μ , n , ρ , and the channel slope θ , the spreading rate of a fixed-volume release and the free-surface profile of the resulting mud flow can be computed from (4.48)–(4.55) and (4.58), and then compared with the measurements. Reasonable agreement between theory and experiments was observed for all runs, and typical results are shown here. Figure 15 shows the free-surface profiles for the following conditions: (a) $C_v = 21.07\%$, $\theta = 18.5^\circ$, $A = 29.2 \text{ cm}^2$, and Reynolds number $Re = \rho u^{2-n} h^n / \mu_n = 0.30$; (b) $C_v = 19.59\%$, $\theta = 24.5^\circ$, $A = 32.4 \text{ cm}^2$, and $Re = 0.11$. Figures 16 and 17 show the spreading rate and hydrographs, respectively, for the following condition: $C_v = 13.05\%$, $\theta = 11^\circ$, and $A = 24.7 \text{ cm}^2$. As expected,

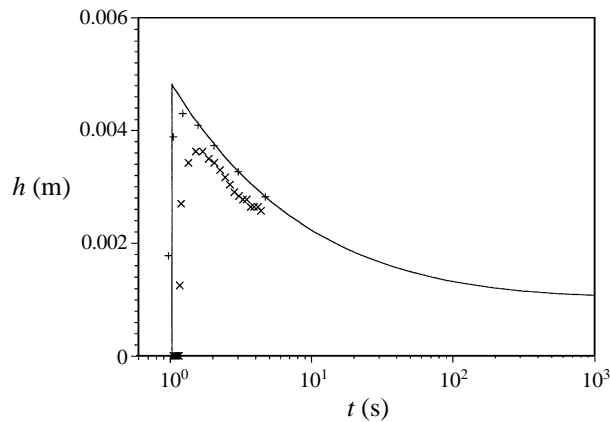


FIGURE 17. Comparison of computed (outer solution: —; composite solution: +) and measured (\times) hydrographs at $x = 0.689$ m.

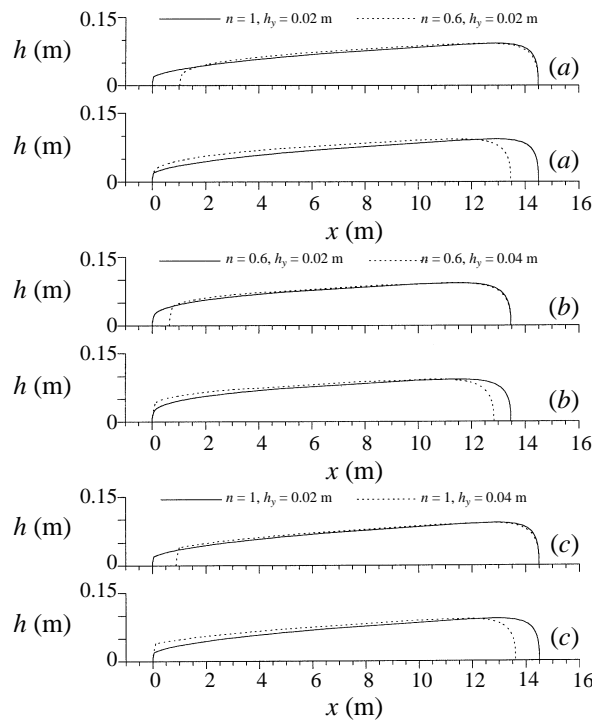


FIGURE 18. Free-surface profiles of mud flows on a slope.

the theory agrees asymptotically well with the observed spreading rate and free-surface profiles.

5. Impact of shear thinning on runout characteristics

To further examine the impact of the shear-thinning phenomenon on mud flows and their final deposits, free-surface profiles of mud flows on a slope are computed by using (4.50), (4.51), (4.53)–(4.55), and (4.58) and shown in figure 18, in which the mud flows are assumed to have a constant volume of $A = 1.0$ m² and to originate from a

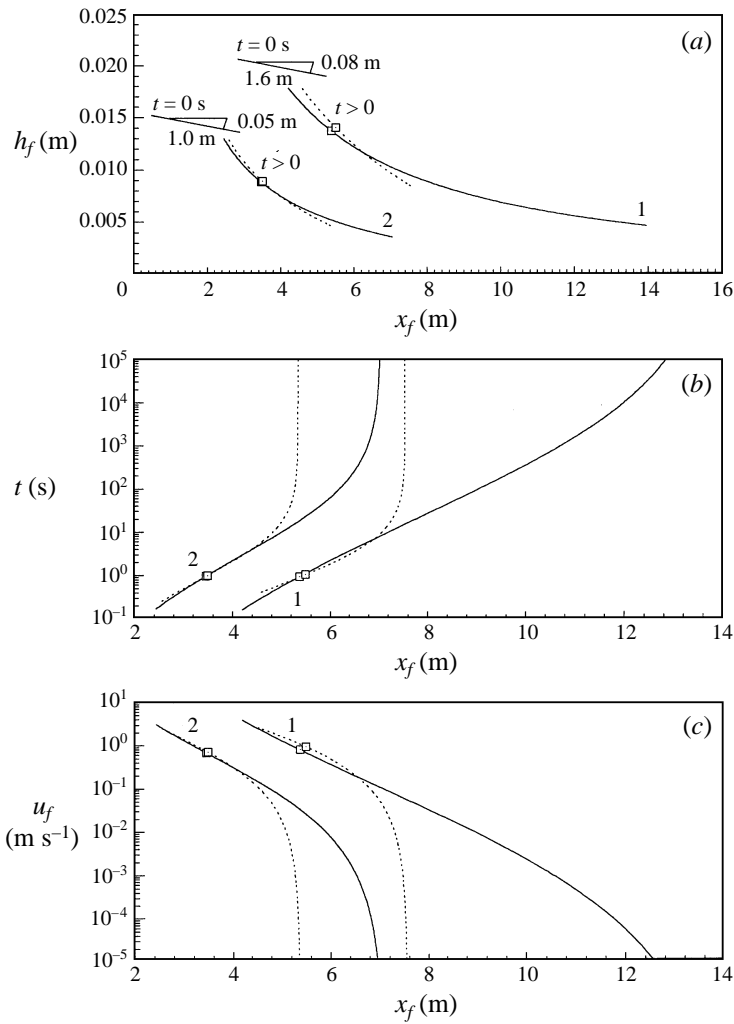


FIGURE 19. Shear-thinning impact on the runout characteristics of a mud flow from a constant-volume source: Herschel–Bulkley model shown as solid lines and Bingham model shown as dashed lines. Rheological data are from table 1, cases (1) and (2). Squares represent the validity boundary. (a) Shock depth versus shock coordinate, (b) shock coordinate versus time, (c) shock velocity versus shock coordinate.

certain upstream source. Four free-surface profiles are compared with each other: (i) $h_y = 0.02$ m and $n = 1$; (ii) $h_y = 0.04$ m and $n = 1$; (iii) $h_y = 0.02$ m and $n = 0.6$; and (iv) $h_y = 0.04$ m and $n = 0.6$. These profiles have the same $h_f (= 0.10$ m) and are spreading down a slope of $\tan \theta = 0.1$. It is seen that for a fixed n , the flow with a large yield depth has a shorter spreading distance and thicker flow depth away from the wave front than that with a small yield depth. If the free-surface profile of a large-yield-stress flow is translated downstream with the leading edges of the fronts coinciding, the flow with a larger yield depth seems to have a lower and flatter wave front than that with a smaller yield depth. It is also seen that for a fixed h_y , the flow with a small value of n has a shorter spreading distance and thicker flow depth away from the wave front than that with a large value of n . If the free-surfaces profile of a small- n flow is translated downstream with the leading edges of the fronts coinciding, the small- n flow seems to have a lower and flatter wave front than the large- n flow. For spreading mud

flows, small values of n seem to have the effect of enlarging yield depth, and this is because n is associated with a sheared flow as indicated in figure 2. However, as far as the final deposit after flow stoppage is concerned, for the same amount of mud, the mud flow with a small yield depth always has a longer runout distance than that with a large yield depth.

The impact of the shear-thinning phenomenon on runout characteristics is apparently obvious but actually complicated, since the shear rate always increases from a minimum of zero at the yield interface to a maximum at the bottom over cross-sections in the history of a mud flow. The local fluid slightly below the yield interface definitely experiences shear thinning, and the local fluid far below the yield interface may experience little shear thinning. During the final decelerating stage, all sheared fluid may experience shear thinning. Herein, this impact is examined in figure 19 by considering two mud flows whose measured rheological data are fitted by the Bingham and Herschel–Bulkley models (see table 1). Our intention here is to compare the two rheological models to see the shear-thinning impact on runout characteristics of mud flows, so any other problems related to small-scale flows are outside the scope of this paper. It is seen that the shear thinning seems not to have much impact on the runout characteristics during early time stages, but does have great impact on runout characteristics during the final decelerating stage as well as on the final deposits. This impact is found to be greater for severe shear-thinning mud flows than for mud flows experiencing slight shear thinning. A Bingham model can provide roughly good results for the runout characteristics of mud flows at the early time stages, and this is contingent on the quality of the fitting of a Bingham model to measured rheological data. Therefore, for highly concentrated mud flows, the Herschel–Bulkley model seems to be a better choice.

6. Summary and application considerations

A formulation has been presented for the dynamics of a two-dimensional, unsteady, laminar, high-density mud flow resulting from a constant-volume mud source on a relatively steep slope (e.g. a mud-slide problem). The Herschel–Bulkley model is chosen to describe the yield-stress, shear-thinning behaviour of the dense mud, and the Newtonian model, power-law model and Bingham model can be treated as special cases of the Herschel–Bulkley model. The boundary-layer approximations with an $O(\eta)$ error are adopted for the flow shortly after its initiation. Physical scaling analysis shows that the kinematic-wave approximation can provide accurate results for the spreading characteristics of low-Reynolds-number flows, having an $O(\varepsilon/\tan\theta)$ error after the wave front has advanced a distance h_f/ε downstream. To improve the free-surface profile near the wave front and hydrographs, further physical scaling analysis shows that the longitudinal pressure gradient term is also important in the region near the wave front. The method of matched-asymptotic expansions is implemented to get asymptotic solutions for the outer region away from and inner region near the wave front, and a composite solution is obtained through a successful matching of the inner and outer solutions, having an $O(\varepsilon/\tan\theta)$ error. The solution depends asymptotically only on the initial mass volume but not on the initial mass distribution, by the fact that the solution for the mud flow originating from a point source is found to be, for the same amount of mud, asymptotically identical to that for the flow from a finite-size source in a dam-burst problem. The flow model can be readily adapted to submarine non-hydroplaning mud flows under deep-water conditions (van Kessel & Kranenburg 1996; Huang & García 1998).

A mud flow of the Herschel–Bulkley type only spreads a finite distance downslope and stops at an equilibrium mud depth with bottom shear stress equal to the yield stress. A large yield stress determines a short runout distance and greatly slows down the flow. The propagation speed of the wave front asymptotically falls to zero, and the final stage of the flow is similar to a creeping motion. The impact of shear thinning on the runout characteristics and final deposit of mud flows is examined. Small values of the flow index ($0 < n \leq 1$) seem to have the effect of both thickening the plug layer of the flow and greatly slowing down the flow. A mud flow with shear thinning in low-shear-rate range may spread far downslope beyond the runout extent estimated by a Bingham model and has a long and thin deposit.

Our experimental results and those of many others have been compared with computational results in different aspects of the theory. The theory is seen to agree well with the experimental results: spreading rate of Newtonian flow (Huppert 1982*a*), free-surface profiles of Newtonian flow (Hunt 1994) and Bingham flow (Liu & Mei 1989; Huang & García 1997*a, b*), and spreading rate and free-surface profiles of Herschel–Bulkley flow in this study. However, it should be noted that the exact shape of the front itself is influenced by the line of contact between two fluids (i.e. mud and air for subaerial flow) and the rigid surface (Greenspan 1978; Hocking 1981), and this is indicated by the curling over at the front tip in figure 12.

The analytical solution is asymptotically valid after the wave front has advanced a certain distance downstream. For mud flows on a slope of 5° , typical of continental slopes, the validity requires that the ratio of the characteristic flow depth to the characteristic flow length be equal to or less than 0.0044 in order to obtain an accuracy within about 5%. This implies that the solution can be used to predict deposits of mud flows which have substantial runout distances (Hampton *et al.* 1996). Although the analytical solution is for two-dimensional mud flows, many flows in nature can be treated simply as two-dimensional if the lateral length scale is many times larger than the vertical length scale (Whipple 1997). To estimate the risk of a future mud flow on an alluvial fan, as an example, the rheological parameters (τ_y, μ_n, n) can be estimated from field surveys or extrapolated/interpolated from rheological measurements in the literature (e.g. Coussot 1997).

More efforts are worthwhile. Comparisons of the solution with both physical (laboratory and field) and numerical results are needed to make a definite statement about the accuracy of the asymptotical solution under other various initial conditions. There must be situations where sediment entrainment and deposition occur, thus entrainment and deposition mechanisms could be included into the model, which would bring in the possibility of self-acceleration.

We would like to thank Professor C. F. Zukoski for opening his laboratory to us for the rheological measurements, and Professor Chiang C. Mei and three anonymous reviewers for their valuable suggestions and comments. Appreciation is extended to Juan Fedele, Jonathan Armbruster, and David Admiraal for this assistance in the experiment. The research was supported by a grant (N00014-93-1-0044) from the Geology and Geophysics Program of the US Office of Naval Research, under the STRATAFORM Program directed by J. Kravitz. This support is gratefully acknowledged.

Appendix A. Approximate equations of motion away from the wave front (outer region)

Here the approximate equations of motion in the outer region are derived, through a scaling process, from the full Navier–Stokes equations. The order of magnitude of the physical scaling is discussed by introducing the following normalizations:

$$x = l_o x^*, \quad y = h_o h^*, \quad p = p^* \rho g h_o \cos \theta, \quad (\text{A } 1 a)$$

$$u = u_o u^*, \quad v = u_o (h_o/l_o) v^*, \quad t = (l_o/u_o) t^*, \quad (\text{A } 1 b)$$

$$(\tau_{xx}, \tau_{yy}) = \mu_n \left(\frac{u_o}{h_o} \right)^n \left(\frac{h_o}{l_o} \right) (\tau_{xx}^*, \tau_{yy}^*), \quad (\tau_{xy}, \tau_{yx}) = \mu_n \left(\frac{u_o}{h_o} \right)^n (\tau_{xy}^*, \tau_{yx}^*), \quad (\text{A } 1 c)$$

where h_o , l_o , and u_o are the characteristic depth, longitudinal length and longitudinal velocity scales, respectively, in the outer region. Thus the normalized continuity and momentum equations are

$$\frac{\partial u^*}{\partial x^*} + \frac{\partial v^*}{\partial y^*} = 0, \quad (\text{A } 2)$$

$$\left(\eta Re \tan \theta \frac{du^*}{dt^*} - \eta^2 \tan^2 \theta \frac{\partial \tau_{xx}^*}{\partial x^*} - \frac{\partial \tau_{yx}^*}{\partial y^*} \right) \left(\frac{n}{2n+1} \right)^n = -\eta \frac{\partial p^*}{\partial x^*} + 1, \quad (\text{A } 3)$$

$$\left(\eta Re \tan \theta \frac{dv^*}{dt^*} - \frac{\partial \tau_{xy}^*}{\partial x^*} - \frac{\partial \tau_{yy}^*}{\partial y^*} \right) \left(\frac{n}{2n+1} \right)^n \eta \tan^2 \theta = -\frac{\partial p^*}{\partial y^*} - 1, \quad (\text{A } 4)$$

where $\eta = \varepsilon/\tan \theta$, $\varepsilon = h_o/l_o$ as defined in (3.1), Re is the Reynolds number defined by (3.11), and $[(2n+1)/n]^n \sim O(1)$ because $1.2 \leq [(2n+1)/n]^n \leq 3$ for $0.1 \leq n \leq 1$. The boundary conditions without external stresses and surface tension are

$$u^* = v^* = 0 \quad \text{at} \quad y^* = 0, \quad (\text{A } 5)$$

$$v^* = \frac{\partial h^*}{\partial t^*} + u^* \frac{\partial h^*}{\partial x^*} \quad \text{at} \quad y^* = h^*, \quad (\text{A } 6)$$

$$p^* \frac{\partial h^*}{\partial x^*} \eta \left(\frac{2n+1}{n} \right)^n - \tau_{xx}^* \frac{\partial h^*}{\partial x^*} \eta^2 \tan^2 \theta + \tau_{xy}^* = 0 \quad \text{at} \quad y^* = h^*, \quad (\text{A } 7)$$

$$-p^* \left(\frac{2n+1}{n} \right)^n + \left(\tau_{yy}^* - \tau_{xy}^* \frac{\partial h^*}{\partial x^*} \right) \eta \tan^2 \theta = 0 \quad \text{at} \quad y^* = h^*. \quad (\text{A } 8)$$

For a slender flow on a very mild slope, it is assumed that

$$\varepsilon \ll 1, \quad \tan \theta \leq O(\varepsilon), \quad \eta \geq O(1), \quad Re \leq O(1/\varepsilon). \quad (\text{A } 9)$$

By expanding all unknowns u^* , v^* , τ_{xx}^* , τ_{xy}^* , τ_{yx}^* , τ_{yy}^* , p^* , h^* in powers of ε , it is readily found that (2.1)–(2.7) represent the leading-order equations and boundary conditions of the physical process, with an error of $O(\varepsilon^2)$. In this case, the inertia terms can be neglected with an error of $O(\varepsilon)$ or $O(\varepsilon^2)$ when $Re \sim O(1)$ or $Re \sim O(\varepsilon)$, respectively.

Herein, a slender flow on a relatively steep slope is considered. The slope is assumed to be so steep that both $\tan \theta \leq O(1)$ and $\varepsilon/\tan \theta \ll 1$ are easily satisfied. Thus, under the conditions

$$\eta \ll 1, \quad \tan \theta \leq O(1), \quad Re \leq O(1/\eta \tan \theta), \quad (\text{A } 10)$$

it can be easily shown that (2.1)–(2.7) represent the leading-order equations and

boundary conditions of the physical problem and that the longitudinal pressure gradient term is negligible, with an error of $O(\eta)$. In this case, the inertia term is negligible when $Re \leq O(1/\tan \theta)$.

Appendix B. Derivation of equation (4.31)

Substituting (4.30a) into (3.4) and use of the chain rule, gives

$$\frac{\partial h_i^*}{\partial t_i^*} + \frac{\partial}{\partial \xi^*} \left[U_i^* h_i^* \frac{\partial \xi^*}{\partial x^*} \right] = 0 \tag{B 1}$$

by the fact that

$$q^* = U_i^* h_i^*. \tag{B 2}$$

Since $\partial x^*/\partial t^* = U_i^*$, (B 1) becomes

$$\frac{\partial h_i^*}{\partial t_i^*} + \frac{\partial}{\partial \xi^*} \left(h_i^* \frac{\partial \xi^*}{\partial t^*} \right) = 0. \tag{B 3}$$

Differentiating $\xi^* = (x^* - x_f^*)/\eta$ with respect to t^* gives

$$\frac{\partial \xi^*}{\partial t^*} = \frac{1}{\eta} \left(U_i^* - \frac{dx_f^*}{dt^*} \right) \tag{B 4}$$

which, when substituted into (B 2), yields (4.31) as

$$\eta \frac{\partial h_i^*}{\partial t_i^*} + \frac{\partial}{\partial \xi^*} \left[h_i^* \left(U_i^* - \frac{dx_f^*}{dt^*} \right) \right] = 0. \tag{B 5}$$

Appendix C. Derivation of (4.43)

From (4.39) and (4.40), we have

$$-\frac{\partial p}{\partial x} + \rho g \sin \theta + \frac{\partial \tau}{\partial y} = 0 \tag{C 1}$$

which is subjected to the boundary conditions (2.4), (2.5), (2.7) and (2.8). It is not difficult to prove that

$$u = \begin{cases} U_p, & h_s \leq y \leq h \\ U_p [1 - y/h_2]^{(n+1)/n}, & 0 \leq y \leq h_s, \end{cases} \tag{C 2}$$

and

$$U = U_p \left(1 - \frac{n}{2n+1} \frac{h_s}{h} \right), \tag{C 3}$$

in which

$$U_p = \frac{n}{n+1} \left[\frac{\rho g h_s^{n+1} \sin \theta \left(1 - \frac{\partial h}{\partial x} \frac{1}{\tan \theta} \right)}{\mu_n} \right]^{1/n}. \tag{C 4}$$

Differentiating (C 2) at $y = 0$ and use of (C 3) yields

$$\left(\frac{\partial u}{\partial y} \right)_{y=0} = \frac{n+1}{n} \frac{(2n+1) U h}{(2n+1) h h_s - n h_s^2}, \tag{C 5}$$

which then gives, when substituted into (1.1),

$$\tau_b = \tau_y + \mu_n \left[\frac{n+1}{n} \frac{(2n+1)Uh}{(2n+1)hh_s - nh_s^2} \right]^n. \quad (\text{C } 6)$$

REFERENCES

- BARNES, H. A. & WALTERS, K. 1985 The yield stress myth? *Rheologica Acta* **24**, 323–326.
- BATCHELOR, G. K. 1967 *An Introduction to Fluid Dynamics*, pp. 216–217. Cambridge University Press.
- BIRD, R. B., DAI, G. C. & YARUSSO, B. J. 1983 The rheology and flow of viscoplastic materials. *Rev. Chem. Engng* **1**, 1–70.
- CHOI, S. U. & GARCÍA, M. H. 1993 Kinematic wave approximation for debris flow routing. *Proc. XXV IAHR Congress, Tokyo, Japan*.
- COSTA, J. E. & WILLIAMS, G. P. 1984 Debris-flow dynamics (videotape). US Geological Survey Open-File Report 84-606, 22.5 mins.
- COUSSOT, P. 1994 Steady, laminar, flow of concentrated mud suspensions in open channel. *J. Hydraul. Res.* **32**(4), 535–559.
- COUSSOT, P. 1997 *Mudflow Rheology and Dynamics*. IAHR Monograph Series, Balkema, 255 pp.
- COUSSOT, P. & PROUST, S. 1996 Slow, unconfined spreading of a mudflow. *J. Geophys. Res.* **101**(B11), 25217–25229.
- COUSSOT, P., PROUST, S. & ANCEY, C. 1996 Rheological interpretation of deposits of yield stress fluids. *J. Non-Newtonian Fluid Mech.* **66**, 55–70.
- CROCHET, M. H. J. & WALTERS, K. 1983 Numerical methods in non-Newtonian fluid mechanics. *Ann. Rev. Fluid Mech.* **15**, 241–260.
- ENGELUND, F. & WAN, Z. 1984 Instability of hyperconcentrated flow. *J. Hydraul. Engng ASCE* **110**, 219–233.
- EVANS, I. D. 1992 On the nature of the yield stress. *J. Rheology* **36**, 1313–1316.
- GREENSPAN, H. P. 1978 On the motion of a small viscous droplet that wets a surface. *J. Fluid Mech.* **84**, 125–143.
- HAMPTON, M. A., LEE, H. J. & LOCAT, J. 1996 Submarine landslides. *Rev. Geophys.* **34**, 33–59.
- HJORTH, P. G. 1990 Stability of free surface sediment flow. *J. Geophys. Res.* **95**(C11), 20363–20366.
- HOCKING, L. M. 1981 Sliding and spreading of thin two-dimensional drops. *Q. J. Mech. Appl. Maths.* **34**, 37–55.
- HUANG, X. & GARCÍA, M. H. 1977a Asymptotic solution for Bingham debris flows. *Proc. 1st Intl Conf. on Debris-Flow Hazards Mitigation: Mechanics, Prediction, and Assessment, San Francisco* (ed. C. L. Chen), pp. 561–575.
- HUANG, X. & GARCÍA, M. H. 1997b A perturbation solution for Bingham-plastic mud flows. *J. Hydraul. Engng ASCE* **123**, 986–994.
- HUANG, X. & GARCÍA, M. H. 1998 Modeling of non-hydroplaning mudflows on continental slopes. *Mar. Geol.* **154** (in press).
- HUNT, B. 1994 Newtonian fluid mechanics treatment of debris flows and avalanches. *J. Hydraul. Engng ASCE* **120**, 1350–1363.
- HUPPERT, H. E. 1982a Flow and instability of a viscous current down a slope. *Nature* **300**, 427–429.
- HUPPERT, H. E. 1982b The propagation of two-dimensional and axisymmetric viscous gravity currents over a rigid horizontal surface. *J. Fluid Mech.* **121**, 43–58.
- HUPPERT, H. E. 1986 The intrusion of fluid mechanics into geology. *J. Fluid Mech.* **173**, 557–594.
- JIANG, L. & LEBLOND, P. H. 1993 Numerical modeling of an underwater Bingham plastic mudslide and the wave which it generates. *J. Geophys. Res.* **98**(C6), 10303–10317.
- JOHNSON, A. M. 1970 *Physical Processes in Geology*. Freeman, San Francisco.
- KEE, D. D. & FONG, C. F. C. M. 1993 A true yield stress? *J. Rheology* **37**, 775–776.
- KESSEL, T. VAN & KRANENBURG, C. 1996 Gravity current of fluid mud on sloping bed. *J. Hydraul. Engng ASCE* **122**, 710–717.

- KRONE, R. B. 1963 A study of rheologic properties of estuarial sediments. *Ser. Rep.* 63–8. Hydraul. Engng. Lab. and Sanitary Res. Lab., Univ. of Calif., Berkeley.
- LI, J., YUAN, J., BI, C. & LUO, D. 1983 The main features of the mudflow in Jiangjia Ravine. *Z. Geomorph. N. F.* **27**, 325–341.
- LIPCOMB, G. G. & DENN, M. M. 1984 Flow of Bingham fluids in complex geometries. *J. Non-Newtonian Fluid Mech.* **14**, 337–346.
- LIU, K. F. & MEI, C. C. 1989 Slow spreading of a sheet of Bingham fluid on an inclined plane. *J. Fluid Mech.* **207**, 505–529.
- LIU, K. F. & MEI, C. C. 1990 Approximate equations for the slow spreading of a thin sheet of Bingham plastic fluid. *Phys. Fluids* **A2**, 30–36.
- LIU, K. F. & MEI, C. C. 1994 Roll waves on a layer of a muddy fluid flowing down a gentle slope – a Bingham model. *Phys. Fluids* **6**, 2577–2590.
- MIGNIOT, P. C. 1968 A study of the physical properties of various forms of very fine sediment and their behavior under hydrodynamic action. *Houille Blanche* **7**, 591–620.
- NAIK, B. 1983 Mechanics of mudflow treated as the flow of a Bingham fluid. PhD thesis. Washington State University.
- NAYFEH, A. H. 1973 *Perturbation Method*. John Wiley & Sons.
- NG, C.-O. & MEI, C. C. 1994 Roll waves on a shallow layer of mud modelled as a power-law fluid. *J. Fluid Mech.* **263**, 151–183.
- NGUYEN, Q. D. & BOGER, D. V. 1992 Measuring the flow properties of yield stress fluids. *Ann. Rev. Fluid Mech.* **24**, 47–88.
- O'BRIEN, J. S. & JULIEN, P. Y. 1988 Laboratory analysis of mudflows properties. *J. Hydraul. Engng. ASCE* **114**, 877–887.
- PIAU, J. M. 1996 Flow of a yield stress fluid in a long domain, application to flow on an inclined plane. *J. Rheology* **40**, 711–723.
- QIAN, N. & WAN, Z. 1986 A critical review of the research on the hyperconcentrated flow in China. Intl Res. and Training Ctr. on Erosion and Sedimentation, Beijing.
- SCHURZ, J. 1992 A yield value in a true solution? *J. Rheology* **36**, 1319–1321.
- SPAANS, R. D. & WILLIAMS, M. C. 1995 At last, a true liquid-phase yield stress. *J. Rheology* **39**, 241–246.
- TAKAHASHI, T. 1991 *Debris Flows*. IAHR Monograph Series. Balkema.
- TROWBRIDGE, J. H. 1987 Instability of concentrated free surface flows. *J. Geophys. Res.* **92**(C9), 9523–9530.
- WAN, Z. 1982 Bed material movement in hyperconcentrated flow. *Ser. Pap.* 31. Inst. of Hydrodyn. and Hydraul. Engng., Tech. Univ. of Denmark, Lyngby.
- WHIPPLE, K. X. 1997 Open-channel flow of Bingham fluids: applications in debris-flow research. *J. Geology* **105**, 243–262.
- WHITHAM, G. B. 1974 *Linear and Nonlinear Waves*. Wiley-Interscience.
- WILKINSON, W. L. 1969 *Non-Newtonian Fluids*. Pergamon.